1958 *Chem. Mater.* **2010,** *22,* 1958–1965
DOI:10.1021/cm902842k

CHEMISTRY OF MATERIALS
Article

Two-Step Sol−Gel Method-Based TiO_2 Nanoparticles with Uniform Morphology and Size for Efficient Photo-Energy Conversion Devices

Sangwook Lee,[†,‡] In-Sun Cho,[†,‡] Ji Hae Lee,[§] Dong Hoe Kim,[†] Dong Wook Kim,[†] Jin Young Kim,[∥] Hyunho Shin,[⊥] Jung-Kun Lee,*[,○] Hyun Suk Jung,*[,§] Nam-Gyu Park,[#] Kyungkon Kim,[▽] Min Jae Ko,[▽] and Kug Sun Hong*[,†,‡]

[†]*Department of Materials Science and Engineering, Seoul National University, Seoul 151-744, South Korea,* [‡]*Research Institute of Advanced Materials, Seoul National University, Seoul 151-744, South Korea,* [§]*School of Advanced Materials Engineering, Kookmin University, Seoul 136-702, South Korea,* [∥]*Chemical and Bioscience Center, National Renewable Energy Laboratory Golden, Colorado 80401,* [⊥]*Department of Ceramic Engineering, Kangnung National University, Kangnung, 210-702, South Korea,* [○]*Department of Mechanical Engineering and Materials Science, University of Pittsburgh, Pittsburgh, Pennsylvania 15260,* [#]*School of Chemical Engineering, Sungkyunkwan University, Suwon, 440-746, South Korea, and* [▽]*Center for Energy Materials, Materials Science and Technology Division, Korea Institute of Science and Technology (KIST), Seoul 136-791, South Korea*

Received September 11, 2009. Revised Manuscript Received February 8, 2010

The performance of dye-sensitized solar cells (DSSCs) consisting of anatase TiO_2 nanoparticles that were synthesized via a two-step sol−gel process was investigated using electron transport and optical characterizations. Spherical nanoparticles with the average diameter of 20 nm, elongated nanorods with an aspect ratio (AR) of 5, and nanowires with AR = 10 were synthesized. The synthesized nanoparticles possess narrow size distribution, high crystallinity, and negligible surface defects and residual organics, which is very suitable for achieving highly efficient photovoltaic devices. The effect of particle size distribution on the performance of DSSC was characterized by comparing the synthesized TiO_2 nanoparticles and commercial TiO_2 nanoparticles (P25). In comparison with P25, the two-step sol−gel-grown nanoparticles significantly improved the photovoltaic conversion efficiency by 32.5%, because of a larger specific surface area, higher electrolyte penetration ability, and lower optical reflectance. Therefore, the photoelectrode of the two-step sol−gel-derived TiO_2 nanoparticles enhanced the adsorption of dye sensitizers (N719), promotes the transfer of photogenerated carriers, and decreases the ratio of reflected solar spectrum that is not harnessed. As a result, the energy conversion efficiency of DSSCs increased to 6.72% without the use of a scattering layer and coadsorbants. We also investigated the effect of aspect ratio of TiO_2 particles on photovoltaic characteristic. An increase in the aspect ratio of the synthesized nanomaterials resulted in an increase in carrier lifetime. A decrease in the density of grain boundaries suppresses the trapping of carriers and the subsequent recombination of electron−hole pairs. This study demonstrates that the two-step sol−gel-derived nanomaterials provide a way to achieve appreciable efficiency of photoconversion devices.

1. Introduction

Nanocrystalline TiO_2 is an interesting material, because of its unique optical and electrical properties, which are suitable for solar energy conversion applications such as photocatalysts, photochromics, and photovoltaics.[1,2] Extensive research on the effect of the shape of TiO_2 nanomaterials has shown that the energy conversion efficiencies of the photovoltaic devices that use nanocrystalline TiO_2 are critically dependent on the morphologies of the nanomaterials.[3−8] The use of one-dimensional TiO_2 nanowires or narrow-size-distributed TiO_2 nanoparticles in dye-sensitized solar cells (DSSCs) is known to improve the charge transfer properties, thereby enhancing the resultant energy conversion efficiencies.[8] In this regard, there has been intensive research into the synthesis of monodispersed TiO_2 nanomaterials with various shapes.

*Authors to whom correspondence should be addressed. E-mail addresses: jul37@pitt.edu (J.K.L.), hjung@kookmin.ac.kr (H.S.J.), kshongss@plaza.snu.ac.kr (K.S.H.).

(1) Grätzel, M. *Nature* **2001**, *414*, 338.
(2) Hoffmann, M. R.; Martin, S. T.; Choi, W.; Bahnemann, D. W. *Chem. Rev.* **1995**, *95*, 69.
(3) Koo, H.-J.; Kim, Y. J.; Lee, Y. H.; Lee, W. I.; Kim, K.; Park, N.-G. *Adv. Mater.* **2008**, *20*, 195.
(4) Zhu, K.; Neale, N. R.; Miedaner, A.; Frank, A. J. *Nano Lett.* **2007**, *7*, 69.
(5) Joo, J.; Kwon, S. G.; Yu, T.; Cho, M.; Lee, J.; Yoon, J.; Hyeon, T. *J. Phys. Chem. B* **2005**, *109*, 15297.
(6) Cho, I.-S.; Kim, D. W.; Lee, S.; Kwak, C. H.; Bae, S.-T.; Noh, J. H.; Yoon, S. H.; Jung, H. S.; Kim, D.-W.; Hong, K. S. *Adv. Funct. Mater.* **2008**, *18*, 2154.
(7) Mao, Y.; Wong, S. S. *J. Am. Chem. Soc.* **2006**, *128*, 8217.
(8) Kang, S. H.; Choi, S.-H.; Kang, M.-S.; Kim, J.-Y.; Kim, H.-S.; Hyeon, T.; Sung, Y.-E. *Adv. Mater.* **2008**, *20*, 54.

Published on Web 02/24/2010

Although conventional synthesis routes such as hydrothermal,[9,10] flame,[11,12] sol−gel,[13,14] and precipitate methods[15,16] are capable of large-scale production, they are not suitable for controlling the shape and size distribution of TiO_2 nanoparticles. The advanced nanochemistries using reverse micelles,[17,18] polyol reactions,[19] and sonochemical reactions[20] have achieved the aforementioned properties. However, these methods restrict the large-scale synthesis of TiO_2.[5] Recently, Joo et al. have found that monodispersed TiO_2 nanorods can be produced on a large scale via a nonhydrolytic sol−gel reaction route.[5] However, this method suffers from residual surface organics and low crystallinity of TiO_2 nanoparticles, both of which are undesirable for harnessing solar energy.[21,22]

Sugimoto recently developed a novel two-step sol−gel process to synthesize TiO_2 nanoparticles[23−30] in large scale (the so-called "gel−sol method"). In this method, oxide particles are synthesized via two steps, i.e., (1) the formation of a hydroxide gel and (2) nucleation and growth to oxide particles.[23,27] Therefore, it is distinguishable from the conventional "sol−gel" method. The two-step sol−gel process is based on an idea of using a highly condensed precursor metal hydroxide gel as a protective matrix against coagulation of the growing particles, as well as a reservoir of the metal ions.[24] Therefore, the TiO_2 nanoparticles with uniform size distribution and various shapes can be obtained. Given that the uniform size distribution of nanoparticles and shape control are essential for improving the catalytic performance of mesoporous materials, it is expected that the photoelectrodes consisting of the TiO_2 nanoparticles that were synthesized via the two-step sol−gel process will promote the transport of optical sensitizers and electrolytes in photovoltaic devices, which would increase their energy conversion efficiency.

In the present study, shape-controlled anatase nanoparticles with uniform morphology and size were synthesized using the two-step sol−gel method. The synthesized nanoparticles possess narrow size distribution, high crystallinity, and clean surface with negligible surface defects such as Ti^{3+} and residual organic compounds, which are very suitable for achieving highly efficient photovoltaic devices. These nanoparticles were used to make photoelectrodes for DSSCs. The effect of uniform spherical TiO_2 nanoparticles on DSSC performance was characterized in comparison with commercial TiO_2 nanoparticles (P25), with an emphasis on their optical reflectance and carrier transport. We demonstrate that the photoelectrode consisting of the two-step sol−gel-based TiO_2 nanoparticles has its unique mesoporous nature which originates from uniform nanoparticles. The uniform pore distribution and large surface area increases the amount of adsorbed dye sensitizers, facilitates the transfer of photogenerated carriers, and enhances the use of the incident solar spectrum. Furthermore, the effect of the aspect ratio of the synthesized nanomaterials on DSSC performance was also investigated from a viewpoint of electron lifetime (i.e., the electron lifetimes increase with the aspect ratio by decrease of grain-boundary density).

2. Experimental Section

Preparation of TiO_2 Nanoparticles.[28] A stock solution of Ti^{4+} (0.5 M) was prepared by mixing titanium isopropoxide (TTIP) and triethanolamine (TEOA) with a molar ratio of TTIP:TEOA = 1:2, followed by the addition of distilled water. The prepared stock solution (pH ~9.5) was then mixed with $HClO_4$ or NaOH solution to adjust the pH of the solution from 8.5 to 10.5. Ethylenediamine (0.4 M; denoted as ED in the current work) was further added as a shape controller. The solution was placed in an autoclave, aged at 100 °C for 24 h (first aging), and further aged at 140 °C for 72 h (second aging). The two-step aging process is essential to obtain uniform TiO_2 nanoparticles, as a hydrolyzed gel network is formed at the first aging step and the nucleation and growth of titania seeds is achieved during the second aging step. The gel matrix plays a decisive role in the second aging to produce the uniform particles (i) as a reservoir of the metal ions to lower the supersaturation for preventing extensive nucleation and (ii) as an anticoagulant fixing the growing particles in the gel matrix.[23] An opaque sol was obtained after the second aging process via transformation from the gel, and the resultant particles dispersed in the sol was washed with and centrifuged from NaOH (six times), HNO_3 (two times), and distilled water (four times) to remove residual organic compounds from the surface of the nanoparticles.

Characterization of Nanoparticles and TiO_2 Films. The morphology of the synthesized nanoparticles was observed by high-resolution transmission electron microscopy (HRTEM) (Model JEM-3000F, JEOL, Tokyo, Japan). The crystalline structures were identified using an X-ray diffractometer (XRD) (Model M18XHF-SRA, MAC-Science Instruments, Yokohama, Japan). The specific surface areas of the TiO_2 nanoparticles and sorption isotherms of TiO_2 films were measured using a Brunauer−Emmett−Teller (BET) analyzer (Model BELSORP-mini II, BEL, Osaka, Japan). Electron binding energies of the synthesized

(9) Yuan, Z.-Y.; Su, B.-L. *Colloids Surf. A* **2004**, *241*, 173.
(10) Nian, J.-N.; Teng, H. *J. Phys. Chem. B* **2006**, *110*, 4193.
(11) McCormick, J. R.; Zhao, B.; Rykov, S. A.; Wang, H.; Chen, J. G. *J. Phys. Chem. B* **2004**, *108*, 17398.
(12) Jiang, J.; Chen, D.-R.; Biswas, P. *Nanotechnology* **2007**, *18*, 285603.
(13) Bischoff, B. L.; Anderson, M. A. *Chem. Mater.* **1995**, *7*, 1772.
(14) Jung, H. S.; Shin, H.; Kim, J. R.; Kim, J. Y.; Hong, K. S.; Lee, J. K. *Langmuir* **2004**, *20*, 11732.
(15) Youn, H. J.; Ha, P. S.; Jung, H. S.; Hong, K. S.; Park, Y. H.; Ko, K. H. *J. Colloid Interface Sci.* **1999**, *211*, 321.
(16) Junin, C.; Thanachayanont, C.; Euvananont, C.; Inpor, K.; Limthongkul, P. *Eur. J. Inorg. Chem.* **2008**, 974.
(17) Stathatos, E.; Lianos, P. *Langmuir* **1997**, *13*, 4295.
(18) Lin, J.; Lin, Y.; Liu, P.; Meziani, M. J.; Allard, L. F.; Sun, Y. *J. Am. Chem. Soc.* **2002**, *124*, 11514.
(19) Feldmann, C.; Jungk, H.-O. *Angew. Chem., Int. Ed.* **2001**, *40*, 359.
(20) Zhu, Y.; Li, H.; Koltypin, Y.; Hacohen, Y. R.; Gedanken, A. *Chem. Commun.* **2001**, 2616.
(21) Wessels, K.; Minnermann, M.; Rathousky, J.; Wark, M.; Oekermann, T. *J. Phys. Chem. C* **2008**, *112*, 15122.
(22) Hou, K.; Tian, B.; Li, F.; Bian, Z.; Zhaob, D.; Huang, C. *J. Mater. Chem.* **2005**, *15*, 2414.
(23) Sugimoto, T.; Okada, K.; Itoh, H. *J. Colloid Interface Sci.* **1997**, *193*, 140.
(24) Sugimoto, T.; Okada, K.; Itoh, H. *J. Disper. Sci. Technol.* **1998**, *19*, 143.
(25) Sugimoto, T.; Zhou, X.; Muramatzu, A. *J. Colloid Interface Sci.* **2002**, *252*, 339.
(26) Sugimoto, T.; Zhou, X. *J. Colloid Interface Sci.* **2002**, *252*, 347.
(27) Sugimoto, T.; Zhou, X.; Muramatzu, A. *J. Colloid Interface Sci.* **2003**, *259*, 43.
(28) Sugimoto, T; Zhou, X.; Muramatsu, A. *J. Colloid Interface Sci.* **2003**, *259*, 53.
(29) Kanie, K.; Sugimoto, T. *J. Am. Chem. Soc.* **2003**, *125*, 10518.
(30) Kanie, K.; Sugimoto, T. *Chem. Commun.* **2004**, 1584.

TiO_2 nanoparticles were analyzed using X-ray photoelectron spectroscopy (XPS) (Sigma Probe, ThermoVG, Hove, U.K.). The XPS spectra were acquired using a monochromatic Al−K source (100 W), and the binding energies of the Ti 2p peaks were calibrated with respect to the C 1s peak from TiO_2 at 284.6 eV. Infrared (IR) transmittance spectra of the synthesized TiO_2 were measured at room temperature in the range of 600−4000 cm^{-1} using an FT-IR spectrometer (Model Nicolet 6700, Thermo Scientific, Waltham, MA). Reflectance and transmittance of the TiO_2 films without dye molecules were measured using ultraviolet−visible light (UV−vis) spectroscopy.

Fabrication of DSSCs and Characterization of Photovoltaic Properties. Porous TiO_2 thick films were screen-printed onto transparent conducting glass [fluorine-doped tin oxide (FTO), Pilkington, England] 1.5 cm × 2 cm in size. The screen-printed films were dried at 80 °C and then were annealed at 450 °C for 1 h.[31] The thickness of the TiO_2 films on the photoelectrodes was measured by a field-emission scanning electron microscope (FESEM) (Model JSM-6330F, JEOL, Tokyo, Japan). A TiO_2 compact layer for blocking backelectron transfer was applied to the high-efficiency cells.[32] The compact layer was formed by spin-coating the TiO_2 polymeric sol, which was prepared using a sol−gel process.[33] The TiO_2 sol, which consists of titanium alkoxide and ethanol, was prepared as follows. Titanium isopropoxide (TTIP, Aldrich, 97%) was dissolved in dry ethanol (Aldrich, 99.9%), and the resulting solution was partially hydrolyzed by adding a mixture of distilled water, nitric acid, and ethanol. The TTIP/H_2O/HNO_3 molar ratio was 1:4:0.04. A final sol was spun on FTO substrates at 3000 rpm for 30 s. The TiO_2 photoelectrodes were immersed in the solution of N719 dye [ruthenium(2,2′-bipyridyl-4,4′-dicarboxylate)$_2$(NCS)$_2$, SOLARONIX, Aubonne, Switzerland, dissolved in ethanol] at 50 °C for 2 h. The dye-adsorbed electrode then was assembled with a platinum counterelectrode to form a sandwich-type dye-sensitized solar cell. A drop of electrolyte solution (Iodolyte AN-50, SOLARONIX, Aubonne, Switzerland) was infiltrated between the two electrodes of the cell. The amounts of the dye that was adsorbed on the photoelectrodes were checked by measuring UV−vis spectra of the desorbed dye solution from the photoelectrodes. The photovoltaic properties of the fabricated solar cells under the illumination of an air mass of 1.5 (with Solar simulator; Peccell Technologies, Japan; intensity: 100 mW cm^{-2}) were measured with the aid of a potentiostat (CHI 608C, CH Instruments, Austin, TX). The light intensity of the solar simulator was calibrated with a reference cell (PV Measurements, Boulder, CO). All the photovoltaic properties were characterized with a mask of 0.55 cm × 0.55 cm, which is 1.2 times larger in area, compared to the active area (0.5 cm × 0.5 cm).[34] Electrochemical impedances of the cells were also measured using the potentiostat with 100 mW cm^{-2} illumination and by applying open-circuit voltage (V_{oc}) as the bias. Response times (electron lifetimes) as a function of time were obtained from the decay of V_{oc} measured by using the open-circuit voltage decay (OCVD) method.[35] For the V_{oc} decay measurements, the incident light was intercepted for a moment, and the transient decay curve of V_{oc} was monitored during relaxation from an illuminated quasi-equilibrium state to the dark equilibrium state. Data points were collected every 50 ms using the aforementioned potentiostat. The electron diffusion coefficient was obtained by the stepped light-induced transient measurements of the photocurrent (SLIM-PC) method[36] with 1 Hz chopped laser illumination (660 nm).

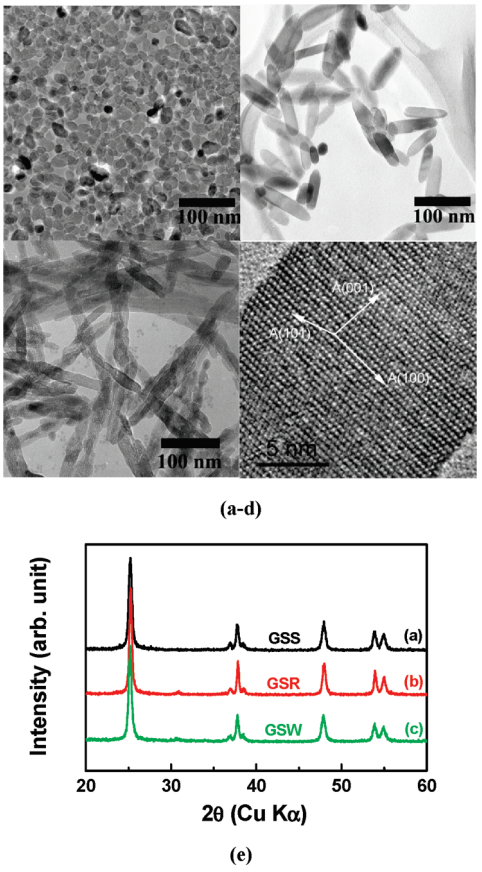

Figure 1. TEM images of the synthesized (a) spherical (GSS), (b) rodlike (GSR), and (c) wirelike (GSW) TiO_2 nanocrystals; (d) HR-TEM image of GSW; and (e) XRD patterns of the synthesized TiO_2 nanoparticles. [The arrows shown in panel (d) indicate anatase crystal lattice directions.]

3. Results and Discussion

3.1. Characterization of Two-Step Sol−Gel Process-Based TiO_2 Nanoparticles. TiO_2 nanocrystals with various aspect ratios were synthesized by controlling the pH and amount of added ED. Figure 1a shows a TEM image of spherical TiO_2 nanoparticles (GSS) with an average diameter of 20 nm, synthesized at an initial pH of 8.5 without ED. Increasing the initial pH to 10.5 changes the product to rod-shaped (GSR) with an average size of 20 nm (width) × 100 nm (length), as seen in Figure 1b. Moreover, the addition of ED doubles the aspect ratio (Figure 1c); the dimensions of the wire-shaped TiO_2 (GSW) are ∼20 nm (width) × ∼200 nm (length). The anisotropic anatase TiO_2 nanoparticles are formed when amino acid groups are adsorbed onto the planes parallel to the *c*-axis of the anatase structure. A $Ti(OH)_4$ gel

(31) Jung, H. S.; Lee, J.-K.; Lee, S.; Hong, K. S.; Shin, H. *J. Phys. Chem. C* **2008**, *112*, 8476.
(32) Ito, S.; Nazeeruddin, K.; Liska, P.; Comte, P.; Charvet, R.; Péchy, P.; Jirousek, M.; Kay, A.; Zakeeruddin, S. M.; Grätzel, M. *Prog. Photovolt: Res. Appl.* **2006**, *14*, 589.
(33) Jung, S. H.; Lee, J. K.; Lee, J.; Kang, B. S.; Jia, Q.; Nastasi, M. *J. Phys. Chem. C* **2008**, *112*, 4205.
(34) Burke, A.; Ito, S.; Snaith, H.; Bach, U.; Kwiatkowski, J.; Grätzel, M. *Nano Lett.* **2008**, *8*, 977.
(35) Zaban, A.; Greenshtein, M.; Bisquert, J. *ChemPhysChem* **2003**, *4*, 859.
(36) Nakade, S.; Kanzaki, T.; Wada, Y.; Yanagida, S. *Langmuir* **2005**, *21*, 10803.

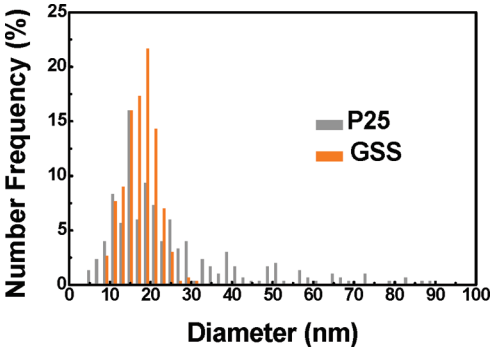

Figure 2. Size distribution gathered from TEM images of P25 and GSS nanoparticles (see Figure S2 in the Supporting Information). Diameters were measured for 300 particles in each sample.

matrix then is crystallized anisotropically.[30] In a high-pH (> 10.5) solution, the amine group strongly bonds to the TiO_2 surfaces, which yields anisotropic nanoparticles. ED, which is a primary amine, is an effective shape controller to yield wire-shaped TiO_2 nanocrystals with a high aspect ratio. The HRTEM image of GSW in Figure 1d indicates that an individual nanowire is an anatase single crystal, and that the nanocrystal has grown along the [001] direction, because of the specific adsorption of ED onto the crystal planes parallel to the *c*-axis. As illustrated in Figure 1e, the XRD patterns of the synthesized TiO_2 nanoparticles show that all of the shape-controlled particles with uniform morphology and size have a pure TiO_2 anatase phase without any secondary phases.

The crystallinity of GSS nanoparticles was compared with commercial P25 nanoparticles and conventional sol−gel grown anatase nanoparticles (see Figure S1 in the Supporting Information). GSS anatase nanoparticles have excellent crystallinity comparable with that of P25, which is much higher than that of the conventional sol−gel-grown anatase nanoparticles. The average particle size was calculated using the Scherrer equation.[37] The sizes of the GSS and P25 nanoparticles are 18.6 and 21.5 nm, respectively. As seen in Figure 2, and in Figure S2 (in the Supporting Information), GSS nanoparticles have a uniform size distribution around the average particle size, whereas the particle size of P25 nanoparticles is widely distributed. The surface defect states and residual organic compounds were characterized using XPS and FT-IR, respectively. As shown in Figure 3a, the binding energies of Ti $2p_{3/2}$ and Ti $2p_{1/2}$ peaks are identical (located at 458.40 and 464.16 eV in both from GSS and P25 nanoparticles), which demonstrates that the concentration of nonstoichiometric defects such as Ti^{3+} ions is negligible in GSS nanoparticles. FT-IR spectra for each sample (see Figure 3b) indicate that the residual amino-acid groups on GSS are easily removed after annealing process (450 °C, 1 h in air), as evidenced by the disappearance of N−H (~1405 cm^{-1}) and N−O (~1340 cm^{-1}) absorbance peaks. The high crystallinity, and negligible surface defects and residual organics from TiO_2 nanoparticles, are a prerequisite for achieving a high efficiency of DSSC.

(37) Cullity, B. *Elements of X-ray Diffraction*, Addision−Wesley: Reading, MA, 1978; p 102.

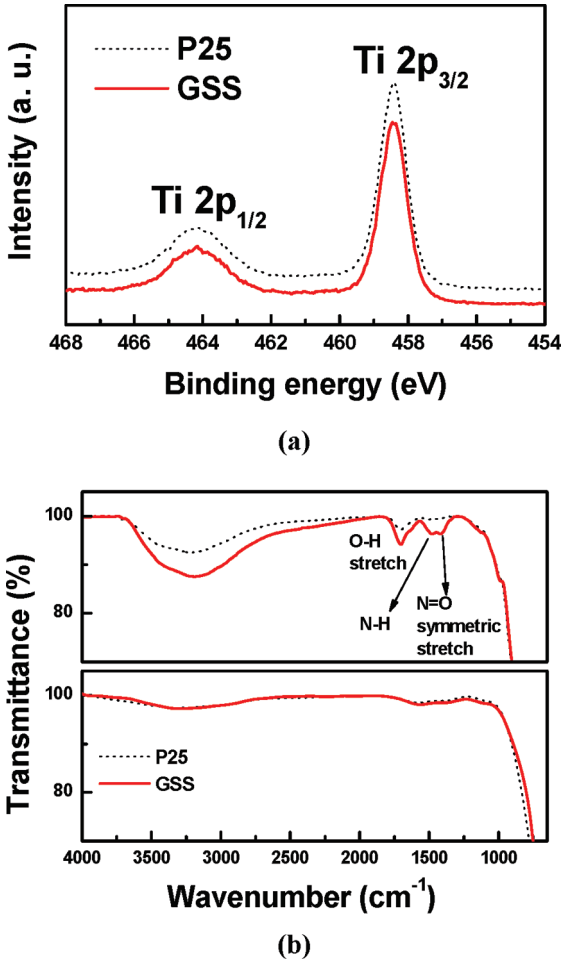

Figure 3. (a) XPS spectra of Ti 2p for P25 and GSS nanoparticles; (b) FT-IR spectra of P25 and GSS before (upper panel) and after (lower panel) annealing at 450 °C for 1 h.

3.2. DSSCs Consisting of Two-Step Sol−Gel-Derived TiO_2 Spherical Nanoparticles. DSSCs were fabricated using GSS and P25 nanoparticles. Because they have similar average particle sizes and crystallinity but different size distributions, the current−voltage ($I-V$) curves in Figure S3 in the Supporting Information represents the effect of particle uniformity on DSSC performance. As summarized in Table 1, the overall conversion efficiency of the GSS-based DSSC is 32.5% higher than that of the P25-based DSSC. The higher energy conversion efficiency of GSS-based DSSC is due to the significant increase in the short-circuit current density (J_{sc}). The J_{sc} value of GSS-based DSSCs is 9.9 mA cm^{-2}, which is higher than the J_{sc} value of a P25-based DSSC (8.3 mA cm^{-2}). First, the larger J_{sc} value of GSS-based DSSCs is attributed to their greater surface area. Given that the thicknesses of the GSS and P25 films are almost identical (~10 μm; see Figure S4 in the Supporting Information), the high specific surface area of the GSS TiO_2 film (see Table 1) is responsible for the increased J_{sc}; the specific surface area of GSS film is 80% larger than that of P25 films (Table 1). Higher specific surface area increases the amount of dye molecules adsorbed on the surface,

Table 1. Specific Surface Area, Dye Amount, and Important Cell Parameters Collected from *J*−*V* Curves[a]

sample	specific surface area ($cm^2\ g^{-1}$)	amount of adsorbed dye ($\times 10^{-7}$ mol cm^{-2})	J_{sc} (mA cm^{-2})	V_{oc} (mV)	FF	η (%)
GSS	74.5	1.08	9.9	728	0.73	5.3
GSR	63.7	0.93	8.3	733	0.77	4.7
GSW	43.1	0.82	7.6	735	0.75	4.2
P25	47.5	0.43	7.4	730	0.74	4.0

[a] All cells used compact TiO_2 (80 nm) as a blocking layer, and the porous TiO_2 films were 10 μm thick.

thereby improving the photon-harvesting capability. If GSS and P25 nanoparticles were packed without agglomeration, the specific surface areas of GSS and P25 films would be 80.0 $m^2\ g^{-1}$ and 71.7 $m^2\ g^{-1}$. However, the BET surface area of P25 films is only 41.5 $m^2\ g^{-1}$, which is much smaller than the calculated value. This indicates that only GSS particles with uniform morphology and size are packed without agglomeration to yield a highly mesoporous structure. In P25 films, smaller nanoparticles fill the pores among larger nanoparticles, leading to the decrease in the surface area during a subsequent thermal annealing process. Figure 4 shows the N_2 sorption isotherms and pore-size distribution (the inset) of the P25 and GSS films. The isotherm loop of GSS film presents a type of type IV isotherm with H1 and H2 types of hysteresis, which is a typical isotherm loop of mesoporous materials containing regular arrays of uniform spherical particles. Such mesoporous materials with a periodic array of particles inherently have a narrow pore-size distribution.[38,39] This is attested by the pore-size distributions of GSS films and P25 films in the inset of Figure 4 showing that the pores of GSS films have a more uniform distribution with the average pore size of 16.3 nm. The mesopore volume percent (mesopore/pore) was 99.3% for GSS films and 93.7% for P25 films, which confirms that GSS films have more interconnected pores than P25 films. Consequently, the dye molecules are more actively transported through the interconnected mesopores, and the amount of adsorbed dye increases in GSS films, compared to the P25 films (see Table 1 and Figure S5 in the Supporting Information).

This uniformly connected nanoparticle network of GSS films also contributes to higher performance of GSS-based DSSCs by improving the electrical carrier transport that is critical in determining the energy conversion efficiency of DSSCs. In this study, the transport of photogenerated carriers was investigated by calculating electron diffusion coefficients from transient photocurrent data (see Figure S6 in the Supporting Information). Figure 5 shows the plots of the electron diffusion coefficients (D) for P25 and GSS photoelectrodes as a function of J_{sc}. It is well-known that the diffusion coefficient

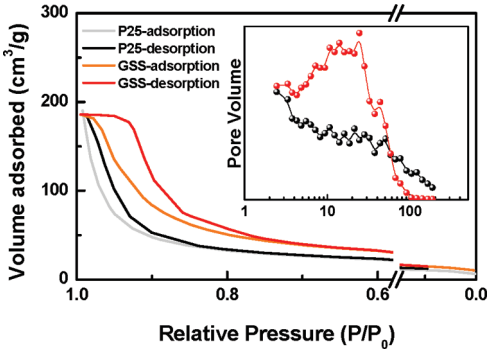

Figure 4. N_2 sorption isotherms and pore-size distribution (inset) determined from P25 and GSS films.

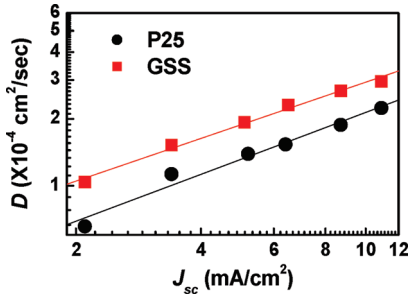

Figure 5. Plots of the diffusion coefficients (D) for P25 and GSS photoelectrodes, as a function of J_{sc}.

increases as the size and crystallinity of TiO_2 nanoparticles, and the ratio of rutile phase to anatase phase, each increase.[40,41] However, P25 photoelectrodes that consist of larger nanoparticles and more rutile phase have a smaller diffusion coefficient than the GSS photoelectrode. Since a negligible difference in the amount of surface defects is found in FT-IR and XPS data, surface trapping cannot explain the difference in the electron diffusion coefficient. We attribute the larger diffusion coefficient of GSS-based DSSCs to the faster reduction of oxidized dye molecules. The interconnected mesopores of GSS films allow easy access of electrolytes to most dye molecules coated on the surface of TiO_2 nanoparticles. Therefore, holes that are produced by the dissociation of excitons quickly react with electrolytes.

The third mechanism of the mesoporous structure to improve J_{sc} is through the change in the optical transmittance. Figure 6a presents the optical reflectance of GSS and P25 films without adsorbed dye at 550 nm as a function of TiO_2 film thickness (see Figure S7 in the Supporting Information). The reflectance of the GSS-based photoelectrode is lower than that of the P25-based one, which can be ascribed to the morphology of the nanoparticles. In the case of an antireflection coating layer, monodispersed silica nanoparticles are used because the particles with narrow size-distribution have a more porous structure than polydispersed particles

(38) Gregg, S. J.; Sing, K. S. W. *Adsorption, Surface Area and Porosity*; Academic Press: New York, 1967; p 7.
(39) Sing, K. S. W.; Everett, D. H.; Haul, R. A.; Moscou, L.; Pierotti, R. A.; Rouquerol, J.; Siemieniewska, T. *Pure Appl. Chem.* **1985**, *57*, 603.
(40) Nakade, S.; Saito, Y.; Kubo, W.; Kitamura, T.; Wada, Y.; Yanagida, S. *J. Phys. Chem. B* **2003**, *107*, 8607.
(41) Hurum, D. C.; Agrios, A. G.; Gray, K. A.; Rajh, T.; Thurnauer, M. C. *J. Phys. Chem. B* **2003**, *107*, 4545.

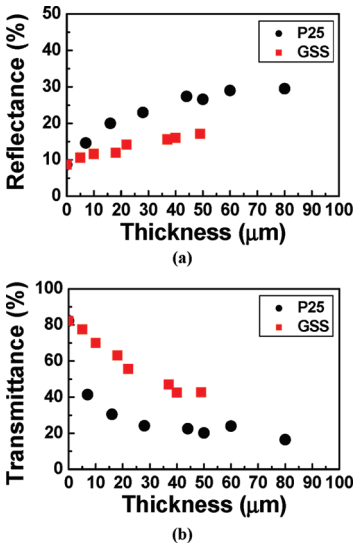

Figure 6. (a) Optical reflectance and (b) transmittance of GSS and P25 photoelectrodes at 550 nm, each as a function of film thickness.

(see the inset of Figure S7 in the Supporting Information).[42,43] Figure 6b presents the optical transmittance of both GSS- and P25-based photoelectrodes at 550 nm, as a function of film thickness (see Figure S7 in the Supporting Information). The GSS film exhibits a higher transmittance than the P25 film in the investigated thickness range. The change in reflectance and transmittance indicates that light scattering is significantly decreased in GSS-based films and solar light penetrates deeper in GSS-based DSSCs than it does in P25-based DSSCs. Therefore, when dye molecules are adsorbed on the surface, the portion of dye molecules contributing to the light harvesting is larger for GSS-based DSSCs. The overall energy conversion efficiency of DSSC, as a function of film thickness [see Figure 7a, and Figure S8 (in the Supporting Information)] demonstrates that the GSS-based DSSCs exhibit higher efficiencies than their P25-based counterparts. From this point forward, the photoelectrodes were fabricated without the compact TiO_2 layer that is usually employed between the porous TiO_2 and TCO layer in DSSCs, to rule out the effect of the compact layer on the reflectance, transmittance, and, finally, cell performance. Note that the efficiency of the GSS-based DSSC increased continually in the investigated thickness range ($\sim$40 μm), whereas the efficiency of the P25-based DSSC saturated at $\sim$30 μm. So far, the superior performance of GSS-based DSSCs is ascribed to the enhancement in dye adsorption, electron transfer, and optical transmittance originating from the mesoporous nature of GSS particle network.

3.3. Effect of Increased Aspect Ratio of TiO_2 Nanomaterials on the Photovoltaic Properties of DSSCs. The morphology of TiO_2 nanoparticles can alter electron transfer properties, thereby influencing the resultant energy conversion efficiencies of DSSCs. Although there have been several studies on the effect of TiO_2 morphologies on photovoltaic performance of DSSCs, the rod-type TiO_2 nanoparticles were too small, compared to the sphere-type nanoparticles[8] or were not sufficiently guaranteed a narrow size distribution.[44] In this study, the synthesized spherical, rodlike, and wirelike TiO_2 nanoparticles exhibit a highly crystalline quality with negligible surface defects, as mentioned, and various aspect ratios (1, 5, and 10) with similar diameters (20 nm), which is suitable for investigating the effect of TiO_2 morphologies on charge transfer in photoelectrodes and, eventually, on energy conversion efficiencies of DSSCs.

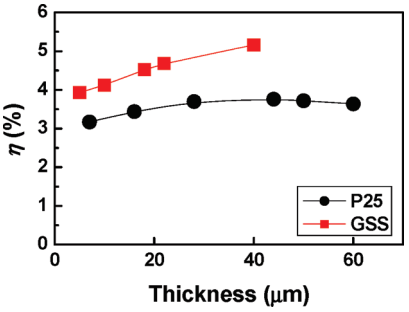

Figure 7. Overall energy conversion efficiency of DSSCs, as a function of film thickness. All photoelectrodes were fabricated without the compact TiO_2 layer to rule out the effect of the compact layer on the reflectance, transmittance, and, finally, cell performance.

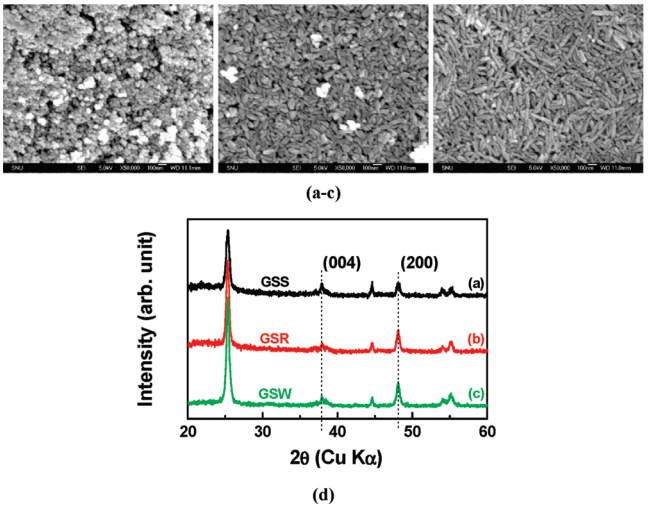

Figure 8. FE-SEM plan-view images of the (a) GSS, (b) GSR, and (c) GSW-based photoelectrode films; (d) XRD patterns of the photoelectrodes.

Figures 8a, 8b, and 8c illustrate the SEM plan-view images of the GSS-, GSR-, and GSW-based photoelectrode films, respectively. The morphology and size uniformity of TiO_2 nanoparticles were not significantly changed after the annealing process. Figure 8d shows the plot of XRD patterns from each photoelectrode, which indicates that the phase transformation from anatase to rutile did not occur during the annealing process. It is noteworthy that the peak intensity ratio of (200), with respect to (004) planes, changes, as a function of particle

(42) Nostell, P.; Roos, A.; Karlsson, B. *Sol. Energy Mater. Sol. Cells* **1998**, *54*, 223.
(43) Nostell, P.; Roos, A.; Karlsson, B. *Thin Solid Films* **1999**, *351*, 170.
(44) Adachi, M.; Murata, Y.; Takao, J.; Jiu, J.; Sakamoto, M.; Wang, F. *J. Am. Chem. Soc.* **2004**, *126*, 14943.

aspect ratio (as shown in Figure 8d). The $I_{(200)}/I_{(004)}$ ratios are 1.0, 2.0, and 2.2 for the films of GSS [aspect ratio (AR) = 1], GSR (AR = 5), and GSW (AR = 10), respectively. The change in the $I_{(200)}/I_{(004)}$ ratio for each TiO_2 film is attributed to the aligned structures of rod and wire particles in each photoelectrode, as evidenced by SEM (see Figures 8b and 8c) and TEM images (see Figure 1d).

To understand the difference in charge recombination rate and electron lifetime for each photoelectrode, electrochemical impedance spectrum (EIS) analysis was performed. Figure 9a shows Nyquist plots (upper panel) of GSS- and GSW-based DSSCs. The impedance components of the interfaces in the DSSCs are observed in the frequency regimes (from left to right) of 10^3-10^5 (ω_1 or ω_2), 10^0-10^3 (ω_3), and 0.1−1 Hz (ω_4). These arcs are assigned to impedances at the conducting layer/TiO_2 (ω_1), Pt/electrolyte (ω_2), or TiO_2/dye/electrolyte (ω_3) interfaces, and to diffusion of the I_3^-/I^- redox electrolyte (ω_4).[45] The ω_3 component (R_3) of GSW-based DSSC was significantly increased compared with that of the GSS-based DSSC. The increase in R_3 is attributed to the following reasons: (i) the decrease in the adsorbed dye molecules (see Table 1) reduces the injected electron density in the conduction band of TiO_2 nanoparticles, thus leading to increased impedance at the TiO_2/dye/electrolyte (ω_3) interface,[45] and (ii) the anisotropic and one-dimensional nanoparticle, that is, the decreased grain boundary density, facilitates the collection of photogenerated electrons from TiO_2 surface to FTO. This retards the recombination between the injected electrons and the electrolyte and increases the impedance (R_3) at the TiO_2/dye/electrolyte (ω_3) interface. Figure 9a also shows the plot of the imaginary part of the impedance as a function of frequency (lower panel) of DSSCs with GSS and GSW TiO_2 photoelectrodes. The maximum frequency in the ω_3 region is defined as $\omega_{max} = (RC)^{-1} \propto 1/\tau$, where R is the resistance, C the capacitance at an electrochemical interface, and τ the electron lifetime.[45−47] The ω_{max} of GSW-based DSSC shifts to lower frequency, compared with that of the GSS-based DSSC, which indicates that the electron lifetime in the wire-type nanoparticles is longer than that in the sphere-type nanoparticles. Moreover, dark current characteristics and electron lifetimes obtained from the decay of V_{oc}, as a function of time, were analyzed to confirm the retardation of carrier recombination in GSW TiO_2 nanoparticles, shown in Figure 9b and 9c. In the case of the GSW-based DSSC, the dark current onset is shifted to a higher potential range, and the electron lifetime is remarkably increased. These results indicate that the use of one-dimensional TiO_2 nanoparticles result in the suppression of the recombination of photogenerated electrons with the electrolyte, which is consistent with the aforementioned EIS analysis.

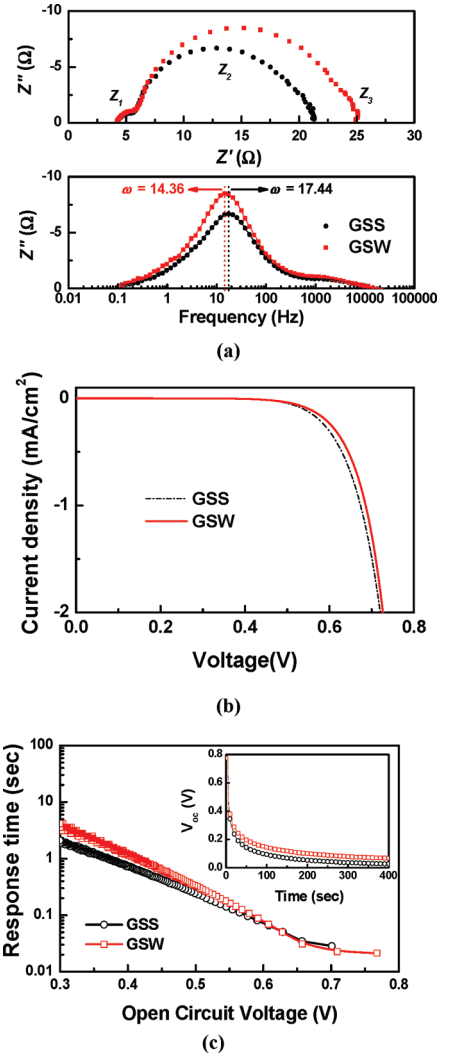

Figure 9. (a) Nyquist plots (upper panel) and the plot of imaginary parts of the impedance, as a function of frequency of GSS and GSW-based DSSCs (lower panel); (b) dark current characteristics of the GSS and GSW-base DSSCs; (c) response times (electron lifetimes) as a function of time.

However, although the wirelike GSW TiO_2 nanoparticles have the advantage of reducing charge recombination, the photovoltaic conversion efficiency of the GSW-based DSSC was much lower than that of the GSS-based DSSC. As summarized in Table 1, the GSW-based DSSC shows lower photocurrent density than the GSS-based DSSC. Therefore, despite the slightly higher V_{oc} and fill factor (FF) for DSSCs composed of anisotropic GSR and GSW nanoparticles, the overall energy conversion efficiency decreases to 4.7% and 4.2%, respectively, whereas that for GSS-based DSSC is 5.3%. The reduced specific surface areas of GSR and GSW nanoparticles are responsible for the low efficiency, because of the decrease in dye adsorption (see Table 1), which leads to a decrease in light absorption.

4. Conclusions

TiO_2 nanoparticles of various shapes were synthesized using the two-step sol−gel method: spherical (GSS),

(45) Hoshikawa, T.; Yamada, M.; Kikuchi, T.; Eguchi, K. *J. Electrochem. Soc.* **2005**, *152*, E68.
(46) Van de Lagemaat, J.; Park, N.-G.; Frank, A. J. *J. Phys. Chem. B* **2000**, *104*, 2044.
(47) Adachi, M.; Sakamoto, M.; Jiu, J.; Ogata, Y.; Isoda, S. *J. Phys. Chem. B* **2006**, *110*, 13872.

rodlike (GSR), and wirelike (GSW) nanoparticles with aspect ratios of 1, 5, and 10, respectively, and their feasibility as the photoelectrode material of dye-sensitized solar cells was investigated. The synthesized anatase nanoparticles were shown to possess high crystallinity, size uniformity, negligible surface defects, and negligible residual organic compounds, all of which are beneficial properties for improved photovoltaic performance. The GSS nanoparticles exhibited a much higher efficiency of the cell than the polydispersed TiO_2 (P25, commercial) because of (i) enhanced dye adsorption, (ii) facilitated charge transport, and (iii) improved optical reflection and transmission properties, which was explained in terms of the mesoporous nature of the GSS-based film with uniform morphology and size. Moreover, the electrons in the GSW showed longer lifetimes than those in the GSS due to enhanced extraction of the photogenerated carriers from the photoelectrode by suppressing their recombination at grain boundaries. The inferior specific surface area of the GSW was interpreted to yield a lower overall cell efficiency than the GSS-based cell. When a blocking layer of optimal thickness was applied on the DSSCs, 6.72% of the overall efficiency (with a mask, 14.38 mA cm^{-2} of J_{sc}, 687 mV of V_{oc}, and FF = 0.680; see Figure S9 in the Supporting Information) was attained for GSS-based DSSCs. Given the absence of a scattering particle layer and of coadsorbants, this result demonstrates that the two-step sol−gel process-derived anatase nanoparticles are very suitable for achieving DSSCs with appreciable efficiency.

Acknowledgment. This work was supported by a Korea Science and Engineering Foundation (KOSEF) grant funded by the Korea government (MEST) (Nos. R01-2007-000-11075-0, R11-2005-048-00000-0, ERC, CMPS and 2009-0065889). This work was also supported by the Nano R&D program through the National Research Foundation of Korea funded by MEST (No. 2009-0082659) and the research program 2009 of Kookmin University in Korea.

Supporting Information Available: Figure S1 shows XRD patterns of the P25, GSS, and sol−gel derived nanoparticles; Figure S2 shows TEM images of the GSS and P25 nanoparticles; Figure S3 shows $J-V$ characteristics of the DSSCs; Figure S4 shows cross-sectional FE-SEM images of the P25 and GSS photoelectrodes; Figure S5 shows the adsorbed dye amounts on the photoelectrodes; Figure S6 shows the transient curves of the current density for the DSSCs; Figure S7 shows reflectance and transmittance of the P25 and GSS photoelectrodes; Figure S8 shows $J-V$ curves, J_{sc}, V_{oc}, and fill factor as a function of the thickness of the P25 and GSS film; Figure S9 shows $J-V$ curve of the DSSC using the GSS photoelectrode with a blocking layer of optimal thickness. (PDF) This material is available free of charge via the Internet at http://pubs.acs.org.